Journal of Biomedical Optics 13(4), 041303 (July/August 2008)

Molecular imaging with optics: primer and case for near-infrared fluorescence techniques in personalized medicine

Eva M. Sevick-Muraca
John C. Rasmussen
Baylor College of Medicine
Department of Radiology
Division of Molecular Imaging
Houston, Texas 77030
E-mail: evas@bcm.edu

Abstract. We compare and contrast the development of optical molecular imaging techniques with nuclear medicine with a didactic emphasis for initiating readers into the field of molecular imaging. The nuclear imaging techniques of gamma scintigraphy, single-photon emission computed tomography, and positron emission tomography are first briefly reviewed. The molecular optical imaging techniques of bioluminescence and fluorescence using gene reporter/probes and gene reporters are described prior to introducing the governing factors of autofluorescence and excitation light leakage. The use of dual-labeled, near-infrared excitable and radio-labeled agents are described with comparative measurements between planar fluorescence and nuclear molecular imaging. The concept of time-independent and -dependent measurements is described with emphasis on integrating time-dependent measurements made in the frequency domain for 3-D tomography. Finally, we comment on the challenges and progress for translating near-infrared (NIR) molecular imaging agents for personalized medicine. [DOI: 10.1117/1.2953185]

Keywords: fluorescence; tissue optics; photon migration; molecular imaging.

Paper 07466SSR received Nov. 17, 2007; revised manuscript received Feb. 20, 2008; accepted for publication Mar. 17, 2008; published online Jul. 24, 2008.

1 Introduction

Emerging personalized health care initiatives are motivated by the need to improve safety, quality, and efficiency of healthcare by addressing individual aspects of a patient's disease state. These initiatives are made possible by the remarkable advances in genomics and proteomics over the past several decades. Indeed, the opportunities to individually diagnose and treat specific diseases through molecular approaches are already a reality rather than a promise for several diseases. For example, several monoclonal antibodies are approved for clinical use including trastuzumab (Herceptin®, Genentech, South San Francisco, CA) and cetuximab (Erbitux®, ImClone, New York, NY), which bind to extracellular portions of the epidermal growth factor receptors EGFr and Her2/Neu that are known to be overexpressed in some cancers and to cause intracellular signaling that leads to cell proliferation and tumor growth and spread. Some small molecules are also being approved for clinical use, such as lapatinib (Tykerb®, GlaxoSmithKline, Philadelphia, PA), which binds to the intracellular phosphorylation domain of EGFr and Her2/Neu to inhibit intracellular signaling. Because these molecular medicines specifically target extracellular receptors, their effective use depends on the expression of target receptors (i.e., EGFr or Her2/Neu) in the diseased state, and the individual's expression levels need to be determined prior to treatment. The individual's expression levels of therapeutic targets for personalized health care are typically determined via biopsy and *in vitro* diagnostics; unfortunately, biopsy is not always possible in all disease states, limiting the use of targeted molecular therapy. Furthermore, disease markers are not always conserved during the course of disease progression (such as during the process of cancer metastasis), causing a spatial and temporal heterogeneity that may create a "sampling" problem for *in vitro* diagnostics of biopsied tissues. One method to circumvent this "sampling" problem is to employ noninvasive, *in vivo* diagnostic molecular imaging to assess potential therapeutic targets and to monitor their levels in response to therapy. While molecular imaging will certainly play a significant clinical role in personalized medicine, its most immediate impact also may be in the drug discovery process by providing a noninvasive method to assess therapeutic responses to drug candidates in preclinical, small animal models of disease.[1–5]

Regardless of whether used in the clinic or preclinical setting, the most simplistic approach to molecular imaging is to label the same targeting moiety used by molecular therapeutic candidates with a "signal generator," administer it in diagnostic rather than therapeutic doses, and image it noninvasively to detect molecularly specific binding and disease marker levels. Currently, nuclear imaging techniques, such as gamma scintigraphy, single photon emission computed tomography (SPECT), and positron emission tomography (PET) offer the "gold-standard" approaches for molecular imaging owing to their exquisite sensitivities to detect femto- to picomolar concentrations of radio-labeled compounds that target disease markers, particularly in deep tissues. Unfortunately, millimo-

---

1083-3668/2008/13(4)/041303/16/$25.00 © 2008 SPIE

lar tissue concentration of iodinated compounds for radiographic contrast, gadolinium agents for magnetic resonance imaging (MRI), and microbubbles for echogenic contrast in ultrasound imaging lessen the usefulness of these conventional techniques for imaging disease marker expression.

In July 2007, we presented a case for molecular imaging with near-infrared (NIR) fluorescence imaging at the Bio-Photonics Summer School in Ven, Sweden. The lectures were intended not to provide a summary of all the recent developments in molecular imaging, but rather to: 1. concisely describe the advantages and disadvantages of optical imaging with respect to nuclear imaging techniques, 2. review the physics and instrumentation of molecular optical imaging techniques, 3. provide a working background for students as well as established investigators who wish to use optical molecular techniques in their studies, and 4. highlight recent results in translational studies. Before introducing optical molecular imaging, we first summarize the established "gold-standard" molecular imaging techniques in nuclear medicine and examples of gene reporter/probe systems for preclinical investigation of therapeutic candidates.

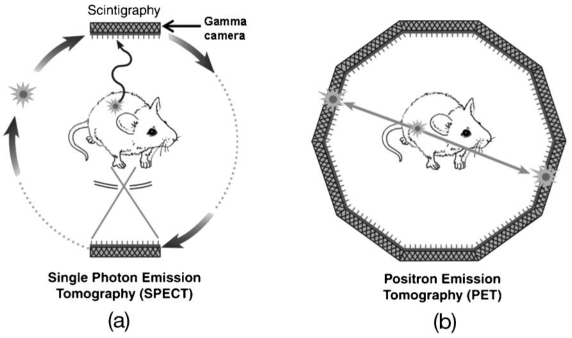

Fig. 1 Schematic of the basic instruments used in molecular imaging with radioisotopes. (a) illustrates a 2-D array of collimated scintillation crystals and PMTs used to image gamma photons. The scintigraphy array (top) produces a 2-D image of the gamma source, while the pinhole aperture on the bottom array restricts the detection of spatially distributed gamma rays such that a series of scintigrams can be used to produce a 3-D reconstruction of the gamma source through single photon emission tomography. (b) illustrates the ring of collimated scintillation crystals and PMTs used to collect coinciding incidents of annihilation photons that are subsequently reconstructed using positron emission tomography algorithms.

2 Molecular Imaging with Nuclear Imaging Techniques

The interested reader can find more authoritative reviews and didactic tests elsewhere,[6,7] but for the purposes of assessing the niche of opportunity for optical molecular imaging, we provide a brief summary review of gamma scintigraphy, SPECT, and finally PET.

The defining feature of nuclear imaging techniques is the use of a radionuclide, which is an unstable, excited nuclide that relaxes and attains stability through alpha, beta, or gamma decay or a combination thereof. Radionuclides that are beta(+) (positron) or gamma emitters are typically used for diagnostic imaging and are generated either by neutral or charged particle bombardment in a reactor or cyclotron. Gamma emitters have a K-shell electron vacancy filled by an electron in the M-shell, producing a gamma ray (also termed a gamma photon) with photon energies typically ranging between 100 to 300 keVs. As illustrated in Fig. 1(a), the spatially discriminated gamma collection can be used to generate a 2-D planar image, called a gamma scintigram, or used to generate 3-D image or tomogram with SPECT. Gamma scintigraphy is the most common clinical nuclear imaging. A gamma camera consists of collimators that direct gamma rays into an array of scintillation crystals, which convert the gamma photons into optical photons that are then detected by photomultiplier tubes (PMTs). Since single photons are collected, the camera is integrated over time, typically over several minutes to generate a planar image. To obtain a 3-D SPECT tomogram, a series of gamma projection images are obtained through a pinhole aperture for image reconstruction through standard back-projection techniques. Because the pinhole aperture restricts the number of gamma rays collected, the acquisition of projections with significant signal-to-noise ratios (SNR) can be time consuming, hence SPECT is typically a lengthy imaging process.

PET imaging is considerably faster than SPECT because all radially emitted photons from all positron decays are collected via a ring of detectors, as shown in Fig. 1(b). During beta(+) decay, a proton is converted into a neutron, producing a positron as well as a neutrino. The emitted positron travels a short distance in the tissue (~ mm dependent on positron energy) before interacting with an electron to produce two 511-keV annihilation photons that travel in opposite directions for coincidence detection. The annihilation photons are detected with scintillation crystals with greater stopping power than used in gamma imaging, and photon counts are registered by PMTs. Coincidence detection enables electronic rejection of single photon events that are not accompanied by the detection of the second annihilation photon within a narrow time window of less than twenty nanoseconds in the array 180 deg from the original detection event. PET imaging is inherently tomographic, and planar imaging akin to gamma scintigraphy is not widely available. There is also no spectral energy differentiation of radionuclides in PET imaging, because only the annihilation photons of 511 keV are collected by PET detectors, regardless of the emitted positron energy.

Common gamma emitters include 99m-Technetium (with a half-life of 6 h), 111-indium (2.8 days), 123-iodine (13.2 h), and 131-iodine (8 days), (A half life is defined as the time required for half of a given amount of radionuclides to decay.) Common positron emitters include 15-oxygen (2 min), 13-nitrogen (10 min), 11-carbon (20 min), 18-fluorine (110 min), 64-copper (12.9 h), and 124-iodine (4.2 days). Targeting compounds can be radio-labeled through isotopic substitution that integrates the radionuclide into the synthesized compound, or as in the case of a radio-metal, through sequestration by a chelating moiety [such as 1,4,7,10-tetraazacyclododecane-*N*,*N*′,*N*″,*N*‴-tetraacetic acid (DOTA), diethylenetriamine-penta-3-carboxylic acid (DTPA), 6-hydrazinopyridine-3-carboxylic acid (HYNIC), or others] that itself is conjugated onto the targeting compound. While the dosage of most conventional imaging agents is based on the weight or moles needed to provide sufficient contrast, radio-labeled agents are administered on the basis of either 1. a becquerel (Bq) that represents the activity of one disintegration per second or 2. a milliCurie (mCi), equivalent to 37 megabecquerels (MBq). As the half-life of the radionuclide approaches, the specific activity (defined in units of mCi per gram or mole of material) of the radio-labeled compound decreases. To obtain or maintain radiologically potent diagnostic imaging agents, close access to a generator or cyclotron is necessary, and isotopic substitution may have to be performed with high doses of radioactivity to achieve sufficient yields of labeled compound for *in-vivo* imaging.

Ex-vivo validation of *in-vivo* gamma, SPECT, or PET images can be achieved by excising tissues and employing autoradiography to count emissions from tissue regions and to coregister with hematoxylin and eosin (H and E) tissue staining. Imaging agent consideration must carefully balance radionuclide half-life with pharmacokinetics. For example, if optimal partitioning to the diseased tissue occurs at times greater than the half-life of the radionuclide, then it is unlikely that the agent will be useful in both preclinical and clinical studies. It is also important to remember that regardless of whether a gamma or positron emitter is used, each radionuclide administered to a subject enables at most one imaging event.

3 Gene Reporter/Probe Systems

To assess the therapeutic impact of gene expression in preclinical studies, gene reporter/probe systems are often employed. A gene reporter is defined as a molecular product of gene expression that innocuously "reports" its expression, but may or may not provide a signal for imaging by itself. Since radionuclides are not naturally occurring in the body, the gene reporter cannot provide a signal for gamma, SPECT, or PET imaging. As a consequence, an exogenous, radio-labeled "probe" of the gene reporter is required to provide the imaging signal. Examples of gene reporter/nuclear probe systems currently in use include: viral thymidine kinase (vTK) and human sodium iodide symporter (hNIS). The vTK enzyme is unique to cells infected with the herpes simplex virus and, because it is not otherwise present in mammalian systems, can be utilized as a gene reporter. When transfected into cells, vTK can be detected following administration of isotopically radio-labeled substrates of the enzyme which, when phosphorylated by the enzyme within vTK expressing cells, accumulate and provide a signal for nuclear imaging.[8–10] These radio-labeled substrates thus act as the probe to provide an imageable signal to identify the gene reporter. Changes in gene reporter expression with therapy can be used to identify the genomic impact of emerging molecular medicines. The hNIS, which is normally and exclusively expressed in the thyroid of mammals to transport iodine, represents a second gene reporter that can be used in combination with preclinical nuclear imaging to assess therapeutic impact on gene expression.[11–14] When hNIS is constitutively expressed as a gene product in cells, the administration of free iodine radionuclides as gene probes results in accumulation of intracellular iodine, providing a nuclear signal for imaging the gene expression via preclinical gamma, SPECT, or PET, depending on the isotope utilized.

It is important to note that most clinically based imaging will probably not depend on gene reporter/probe systems, since they require *in-vivo* gene transfection to be done to produce the gene reporter needed for imaging. (An exception may be the use of nuclear imaging of vTK substrates to assess efficacy of "suicide" gene therapy. When vTK is expressed preferentially in cancer cells, the administration and accumulation of prodrugs (such as ganciclovir) that become cytotoxic when phosphorylated by vTK enables a therapeutic approach. The opportunity to use exogenous "probes" that are radio-labeled substrates of vTK can enable monitoring of transfection efficiency and monitoring response to vTK gene therapy.) Instead, clinical molecular imaging will probably depend on the administration of radio-labeled probes to target existing endogenous gene products. In nuclear imaging, the most common probe of endogenous markers is 18-F-fluoro-2-deoxy glucose (18-F-FDG), which is taken up by the glucose transporters (GLUTs) and shuttled across the plasma membrane for phosphorylation by the hexokinase pathway. After phosphorylation, the 18-F-FDG is trapped and cannot be further processed. Hence 18-F-FDG accumulates in highly glycolytic cells and provides molecular imaging of highly glycolytic tissues, such as the heart wall and some cancers. Unfortunately, glycolysis and GLUTs are ubiquitous, and while 18-F-FDG may provide metabolic information and hence a general response to therapy, FDG-PET does not provide molecularly specific information of disease markers. Nonetheless, FGD-PET provides a first step for molecular diagnostics of therapeutic response in highly glycolytic tissues, and represents the first molecular imaging agent for preclinical as well as clinical study.

Whether used preclinically or clinically, issues of radionuclide half-life and logistical (safety and production) considerations provide challenges for molecular imaging that may be overcome with optical techniques. In the following, we review molecular imaging with optical techniques, namely bioluminescence and fluorescence techniques.

4 Molecular Imaging with Optical Imaging Techniques

In molecular imaging, there are generally two types of noninvasive optical imaging techniques employed primarily in preclinical, small animal imaging studies: bioluminescence and fluorescence imaging. Bioluminescence is dependent on a gene reporter/probe system.[15] The firefly or Renilla (sea pansy) luciferase enzyme is not normally expressed in mammalian cells, but when exogenously and innocuously introduced as a gene reporter, it can be imaged optically on the administration of D-luciferin or coelenterazine as a probe of its luciferase gene expression. On oxidation of its substrate, light of 500 to 580 nm is produced and collected via a charge-coupled device (CCD) camera as depicted in Fig. 2(a). Similar to radionuclides, there is one photon imaging event per molecule of D-luciferin or coelenterazine oxidized and, as a consequence, photon count rates can be considered similar to nuclear techniques. Unfortunately, ambient light can create a significant noise floor for bioluminescence, requiring the use of "light-tight" measurement systems and restricting hybrid tomography systems (see Sec. 7). Otherwise, bioluminescence measurements have low background signals, since there are no other endogenous luminescence sources. Figure 3 illustrates the typical use of bioluminescence in a preclinical imaging study in which a breast cancer cell line, SKBr-3, is

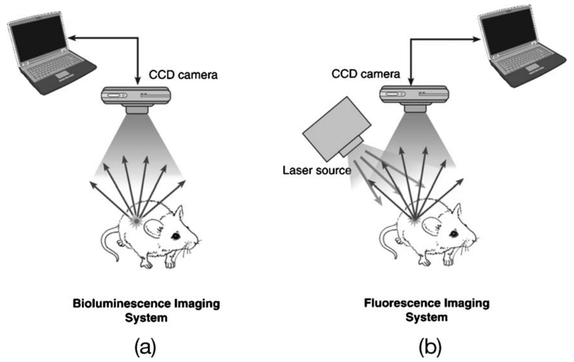

Fig. 2 Schematic of the basic instrumentation used for molecular optical imaging. (a) illustrates a basic bioluminescence imaging system in which a CCD camera collects bioluminescent photons. (b) illustrates the basic setup required to image fluorescent photons. The laser source is required to excite the fluorophore, thus producing a red-shifted emission signal detected by the CCD camera.

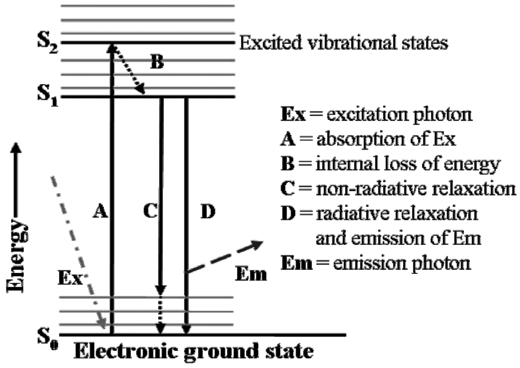

Fig. 4 A Jablonski diagram illustrating the fluorescence process in which an excitation photon (Ex) is absorbed, causing the fluorophore to enter a higher vibrational state. If the fluorophore undergoes radiative relaxation (D), an emission photon is emitted. The fraction of absorbed photons that are reemitted as fluorescence is known as the quantum efficiency.

transfected to stably produce luciferase for the purposes of tracking tumor growth. Five minutes prior to imaging, the animal is injected with 100 μL of 100-μM D-luciferin. On acquiring photon counts over 5 min of integration time, the bioluminescence photon counts are overlaid on the white light photograph of the animal, providing an indication of tumor location. Over time, bioluminescence can provide a rate of tumor growth or regression in response to therapeutic drug candidates.

In contrast to nuclear and bioluminescent techniques, the generation of fluorescent gene reporters affords the ability to directly measure gene expression without the use of an exogenous probe. The expression of an innocuous green or red fluorescent protein as a gene reporter directly enables an optical signal. Another distinguishing feature of fluorescent gene reporters is the requirement of an excitation light source that typically illuminates the entire animal, as shown in Fig. 2(b). The incident excitation light can repeatedly reactivate fluorescent proteins to provide high photon counts for imaging. As shown in the Jablonski diagram in Fig. 4, after activation by excitation light, the subsequent relaxation back to the ground state can occur through one of two pathways. The first pathway (C in Fig. 4) involves the nonradiative relaxation of the fluorophore, while the second pathway (D in Fig. 4) generates a fluorescent photon, with a smaller energy and longer wavelength than the excitation photon. The quantum efficiency is defined as the ratio of the radiative events to the absorption events. Once the fluorescent protein is in the ground state again, it is immediately available for reactivation by the tissue-penetrating excitation light. If one considers a fluorescent protein with a nanosecond fluorescent lifetime (i.e., the mean time between absorption of an excitation photon and subsequent radiative relaxation to the ground state) and a quantum efficiency of one tenth, then the theoretical limit of the number of imaging photon events per fluorophore could be 100,000 photons per second! There are a number of other factors that prevent the realization of a nearly billionth-fold greater sensitivity of fluorescence over "gold-standard" nuclear techniques, including, in order of importance: photobleaching, autofluorescence, and excitation light leakage.

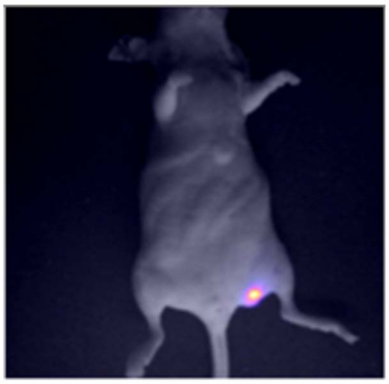

Fig. 3 Bioluminescence in a preclinical model of a breast cancer cell line (SKBr-3) transfected to produce luciferase. The bioluminescent image was obtained five minutes after IV injection of 100 μL of 100-μM D-luciferin. The bioluminescent image was acquired with five minutes of integration time and is overlaid on the white light image. Image reproduced from Sampath et al.[25] (Color online only.)

Photobleaching can be a problem in microscopy and with some fluorophores such as protoporphyrin IX, but is not a substantial problem in optical imaging of tissues, since the relatively low powers of excitation light in properly designed imaging devices are too small to create population inversion or photon destruction of many fluorescent proteins or dyes. While frequently cited as the reason for using inorganic quantum dots over organic dyes, photobleaching is typically not a concern or a limitation for collecting high photon counts from most organic fluorescent proteins or exogenous dyes when illuminated by broad beam or diffuse excitation sources.

Autofluorescence is an undesired fluorescent signal that emanates from endogenous fluorophores within the system of interest. Depending on the excitation wavelength, autofluorescence can be generated from various organic molecules that are present naturally in the tissue or that were consumed in the animal's diet. The high background signals arising from autofluorescence raise the noise floor and hence the limit of detectable tissue concentrations of fluorescent gene reporters as well as exogenous fluorophores. Unless the signal owing to the fluorescent reporter is greater than the noise floor, it can-

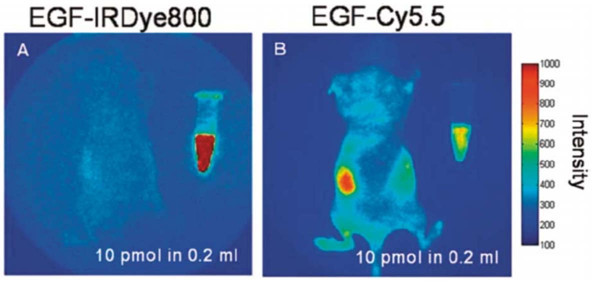

Fig. 5 Comparison of autofluorescence at two excitation wavelengths: (a) autofluorescence levels in a mouse illuminated with 780-nm excitation light. A vial containing 50 nM of EGF-IRDye® 800 cw is also illuminated for comparison; (b) autofluorescence levels in a mouse illuminated with 690-nm excitation light. A vial containing 50 nm of EGF-Cy5.5 is also illuminated for comparison. The autofluorescence in (a), the NIR image, is significantly lower than that in (b) the red fluorescent images. Adapted from Adams et al.[28]

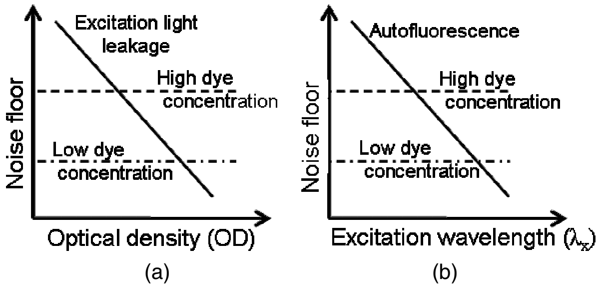

Fig. 6 Schematic illustrating the general trends of the major noise floor contributors in optical imaging. (a) As the optical density of the filters increase, the intensity of the excitation light leakage decreases, thus permitting lower concentrations of dye to be seen. (b) As the excitation light wavelength increases, the intensity of the autofluorescent signal decreases, also permitting lower concentrations of the desired fluorophore to be imaged.

not be detected. For example, Fig. 5(a) depicts the fluorescent image acquired at wavelengths >710 nm of a native mouse without any exogenous agent while illuminated with 690-nm light.[16] Beside the mouse is a vial containing 50 nM of Cy5.5, a 690-nm, red-excitable fluorescent dye. Clearly, the noise floor due to autofluorescence from 690-nm excitation is significantly greater in the mouse than that offered by the signal due to 50 nM of Cy5.5. The image clearly illustrates that the noise floor owing to autofluorescence prevents the imaging of tissue concentrations of fluorescent gene reporters at ⩽50 nM at these excitation and emission wavelengths. In contrast, on illuminating the animal at a NIR excitation wavelength of 780 nm, the fluorescent image taken at >830 nm in Fig. 5(b) shows than the noise floor owing to autofluorescence in the mouse is substantially lower than the signal arising from a vial of 50 nM of indocyanine green, a NIR excitable dye. As one approaches the NIR wavelength regime (with excitation light >750 nm), tissue autofluorescence contributes significantly less to the autofluorescent background, and the noise floor for detecting gene reporters and exogenous dyes dramatically reduces. Unfortunately, there are no natural proteins that excite and emit in the NIR wavelength regime; thus the noise floor due to autofluorescence can always be expected to limit the sensitivity of fluorescent gene reporters. It is also noteworthy that because bioluminescence imaging does not use an excitation source, no autofluorescence background exists to contribute to its noise floor.

Excitation light leakage creates another significant noise floor for fluorescence imaging that is not present in bioluminescence imaging. As shown in the fluorescence imaging schematic depicted in Fig. 2(b), animals are illuminated with an excitation source that generates a significant backscattered signal that must be spectrally separated from the vanishingly small fluorescent signal arising from the fluorescent gene reporter or exogenous dye. Optical filters used to reject excitation light and pass fluorescent light typically reject 3 to 6 orders of magnitude of collimated incident excitation light. Often, however, this level of rejection is not sufficient to enable detection of low levels of fluorescent proteins or probes.[17] For example, consider a fluorescent gene reporter or probe at tissue concentrations that give rise to 10^5 photons/cm^2/sec at the tissue surface. The excitation light scattered from the surface generates 10^{12} backscattered photons/cm^2/sec. If using an interference filter with an optical density of 6 at the excitation wavelength, then a ten-fold greater excitation than emission signal will be collected at the detector, and excitation light leakage will obscure the fluorescence from the gene reporter or probe in the absence of contributions from autofluorescence. Typically, the performance capabilities of interference filters are worse than manufacturer specifications because 1. the excitation light is often not monochromatic, making it difficult to effectively use holographic rejection filters that are wavelength specific; and 2. the light impinging on the filter is not normally incident, changing the rejection capability of the interference filters. In Sec. 7, we describe our approach to minimize the impact of excitation light leakage for sensitive fluorescence imaging.

To capitalize on low-level fluorescent imaging, particularly in orthotopic regions, the overall noise floor must be minimized. As illustrated in Fig. 6(a) the excitation noise floor decreases as the optical density of the excitation rejection filters increases. Likewise, the noise floor of the autofluorescence decreases as the excitation wavelength increases, as shown in Fig. 6(b). By optimizing the excitation wavelength and its corresponding rejection filters, the overall noise floor is reduced, enabling the acquisition of smaller and/or deeper fluorescent signals.

To summarize this section, optical imaging with bioluminescence and fluorescence using a gene reporter/probe or simply a fluorescent gene reporter may add significant flexibility over nuclear imaging if issues of the noise floors can be overcome. Unfortunately, the need to introduce a foreign gene product significantly restricts translation into the clinic, and the bioluminescence techniques are best employed for preclinical studies. In the next section, we describe NIR fluorescence enhanced optical imaging that uses an exogenous probe to assess endogenous disease markers and that has the potential for clinical translation.

5 Molecular Imaging with Near-Infrared Fluorescence Imaging

As described earlier, the use of NIR excitation light is advantageous because little or no autofluorescence provides for a low background floor. Indocyanine green (ICG) is commonly used as a NIR dye in phantom and animal studies, as it can be excited at 785 nm, and the fluorescence at 830 nm and above provides a sufficient Stoke's shift to be efficiently collected. The dye, sold as IC-Green (Akorn Pharmaceuticals, Buffalo Grove, Illinois), is approved for intravenous administration, at 2 mg/kg for use in hepatic clearance as well as assessing retinopathy studies. However, ICG does not have a functional group for conjugation to molecularly targeting entities such as antibodies, aptamers, or peptides. Instead, the agent associates with albumin in the blood, and as described in Sec. 8, provides a unique opportunity to translate NIR instrumentation into vascular imaging. Recently, a number of NIR excitable fluorophores with functional groups for conjugation have become commercially available, (i.e., AlexaFluor750 from In-Vitrogen, Carlsbad California; IRDye 800CW, Li-Cor, Lincoln Nebraska; and Cy7.5, Amersham/GE Healthcare, Piscataway, NJ), thus expanding the opportunities for NIR molecular imaging. Unfortunately, none are approved for human use.

With the removal of the noise floor associated with autofluorescence, the opportunity to assess the sensitivity of NIR molecular imaging can be evaluated in small animal models using dual-labeled imaging agents. Dual labeling involves the conjugation of a NIR fluorophore as well as a chelating moiety for sequestration of a radio metal for nuclear imaging. Dual-labeling a single targeting moiety provides an accurate and convenient method to compare sensitivities of nuclear and optical imaging agents as well as an inherent validation for translational studies (see Sec. 8). Recently, Wang et al. have dual labeled a number of entities for targeting the interleukin-11 receptor expressed on metastasizing cancer cells,[18] the $\alpha_v\beta_3$ integrin associated with tumor angiogenesis and melanoma cancer cells,[19–24] and trastuzumab for targeting Her2/Neu positive breast cancer metastasis in lymph nodes[25] (see article in this series by Sampath et al.). As an example of dual-labeled imaging, Fig. 7(a) contains the white light, Fig. 7(b) the gamma scintigram, and Fig. 7(c) the fluorescence-enhanced optical image of a typical nude mouse bearing an integrin-positive human melanoma tumor (M21) in the left hind limb (right side: anterior view is displayed by figure) and an integrin-negative (M21-L) tumor in the right hind limb (left side: anterior view is displayed by figure). The digital photo of the animal depicts the regions of interest (ROIs) selected for the collection of intensity signals from 5 nmol and 90 μCi of integrin targeted111-DTPA-Lys(IRDye800)-c(KRGDf) administered 24 h prior to imaging. The nuclear and optical images show a low signal in the negative (M21-L) tumor (left side); a high signal in the liver and bladder indicating wash-out of the dye, and a high signal in the integrin positive (M21) tumor (right side). It is noteworthy that optical imaging after 800 msec of CCD camera integration time provides better contrast of M21 than the planar scintigraphy of the same animal after 15 min of gamma camera integration time. The comparative results are performed using planar fluorescence imaging for direct comparison to gamma scintigraphy, and quantitatively show that the target-to-background ratio (TBR) from both scintigraphy and fluorescence images are statistically similar, while the SNR of the fluorescence is significantly higher than that from scintigraphy due to scintigraphy's higher noise floor.[20] Furthermore, this work showed that NIR fluorescence imaging requires lower contrast compared to gamma scintigraphy to achieve a comparable SNR. Similar results are reported by Sampath et al.[25] While these results are the first to demonstrate comparable sensitivity of NIR fluorescence to the gold standard of nuclear imaging, it is important to note that they also evidence the improvement in SNR owing to the increased photon count with fluorophores. While NIR fluorescence imaging can be expected to have higher background noise associated with imperfect rejection of scattered excitation light, the increased photon count may more than compensate to result in a net improvement in SNR. Of course, this comparison has been made on the surface of a small animal, and as the fluorescent signal is generated deeper within the tissue, the attenuation of NIR excitation and fluorescent light may challenge the photon count rate and hence lessen the contrast and SNR of the fluorescent images. However, as long as the noise floor is not approached (i.e., excitation light leakage and autofluorescence kept to a minimum below the signal levels), the ability to integrate a CCD camera over longer times may compensate for reduced photon count rates associated with light attenuation, which might be expected in deep tissue fluorescence enhanced optical imaging.

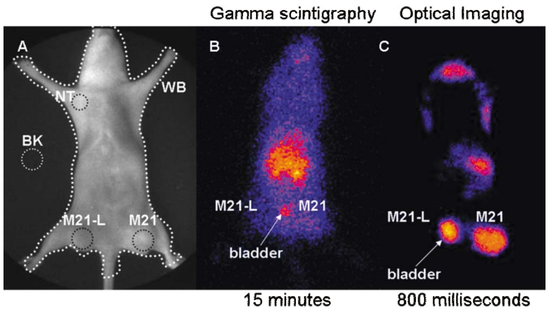

Fig. 7 (a) White light, (b) nuclear scintigram, and (c) fluorescence-enhanced optical image of a typical nude mouse xenograph bearing an integrin-positive (M21) tumor in the left thigh (right side: anterior view is displayed by figure) and an integrin-negative (M21-L) tumor in the right thigh (left side: anterior view is displayed by figure). The digital photograph of the animal depicts the ROIs selected for the collection of intensity signals either in the positive tumor, negative tumor, or normal tissue regions. The nuclear and optical images show a low signal in the negative (M21-L tumor left side), a high signal in the bladder indicating wash-out of the dye, and a high signal in the integrin positive (M21 tumor right side). The optical image was plotted in a pseudo-color format for enhancement of the intensity scale in the tumor and background. The nuclear image was also adjusted with the same color scale for better discrimination between the several levels of gray provided by the 16-bit image. The nuclear image was acquired after 15 min of integration, whereas the optical image was acquired for a total exposure time of 800 ms. Adapted from Houston et al.[20] (Color online only.)

Other dual-labeling studies have been conducted recently. Using cypate (which is structurally similar to ICG) conjugated to a DOTA chelating moiety, Zhang and Achilefu[26] demonstrated that the fluorescent properties can be retained in dual-labeled agents, a finding that is also substantiated by the *in-vivo* imaging work described earlier. Similar to the study by Sampath et al.,[25] Xu et al.[27] dual-labeled trastuzumab with a red-excitable dye, Cy5.5, as well as with chelating moiety for

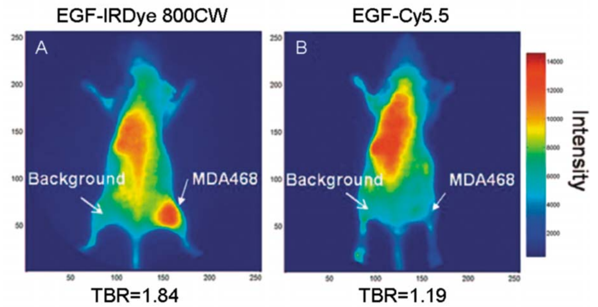

Fig. 8 Comparison of target-to-background ratio (TBR) in two different dye conjugates 24 h after injection in MDA-MB-468 tumor-bearing mice. Images of mouse with an injection of 1 nmol of (a) EGF-IRDye® 800 cw and (b) EGF-Cy5.5. (a) NIR dye conjugate has significantly higher TBR than (b) red fluorescent dye. Adapted from Adams et al.[28] (Color online only.)

eventual use in preclinical studies. Unfortunately, the use of the red-excitable dye will entail a high noise floor, owing to autofluorescence, and may prevent the sensitivities required for noninvasive optical imaging. To illustrate the impact on the choice of fluorophore, Adams and co-workers[28] labeled the epidermal growth factor that is a ligand to EGFr with both IRDye800 CW (a NIR fluorophore with excitation and emission at 785 and 830 nm, respectively) and Cy5.5, (a red-excitable fluorophore with excitation and emission at 690 and 710 nm, respectively), and administered the agents in separate animals bearing a breast cancer cell line that expressed EGFr (Fig. 8). Their results show that TBR was substantially improved when the NIR, as opposed to the red-excitable fluorophore, was conjugated to the peptide, presumably due to a reduction of the background signals owing to autofluorescence. Using targeting ultrasmall iron oxide particles, a number of investigators have also dual-labeled with Cy5.5 to compare fluorescence optical imaging with MRI.[29] Again, the noise floor associated with autofluorescence may reduce the sensitivity. While spectral unmixing[30] may enable some segregation of autofluorescence from the fluorophore, quantitative studies to show conservation of TBR and SNR with spectra unmixing of high background signals remain to be performed. It may simply be easier to employ NIR instead of red-excitable dyes to reduce the background rather than add the additional instrumentation required to perform spectral unmixing.

Given the ability to image comparable signals from targeting compounds conjugated to NIR fluorophores and from those conjugated to chelating moieties for radio-metal sequestration, NIR optical imaging clearly has the opportunity for molecular imaging with fluorescently labeled exogenous probes. Certainly with the increased photon count rate, comparable TBR, and superior SNR, as compared to the low photon count rates of SPECT and PET, opportunities for NIR tomographic imaging are evident. In the following sections, we first describe the instrumentation associated with NIR fluorescence tomography, and then the algorithmic approaches for both small animal tomography and for tomography in clinically relevant volumes.

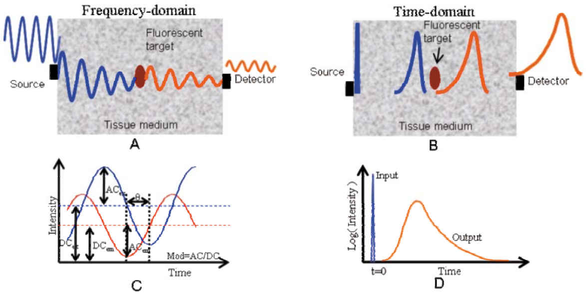

Fig. 9 Examples of type of input and detected signals for (a) and (c) frequency- and (b) and (d) time-domain measurements. (a) Propagation of intensity modulated excitation light undergoes amplitude attenuation and phase shift as it propagates through the tissue medium. The generated fluorescent signal modulates at the same frequency and undergoes further amplitude and phase attenuation as it propagates to the detector. (c) Comparison of the initial input signal to the detected signal with the measurable ac, dc, and θ components. (b) Illustration of the broadening of a pulse of excitation light as it propagates across the tissue. The generated pulse of fluorescence light also broadens as it propagates to the detector. (c) Comparison of the initial input signal to the detected signal. The ac and θ components can be obtained via Fourier transform.

6 Instrumentation for Near-Infrared Tomography

Optical fluorescence measurements are possible using time-independent or time-dependent techniques. Time-independent or continuous wave (cw) techniques employ the simplest instrumentation and consist of an excitation source to illuminate the tissue surfaces and a camera to collect the re-emitted fluorescent intensity, as illustrated previously in Fig. 2(b). In cw imaging, the detected intensity is a function of not only the amount and location of fluorophore present in the tissues, but also the local optical attenuation properties. While useful for planar fluorescent imaging, time-invariant techniques do not take advantage of the contrast offered by photon “time of flight” or fluorescent lifetime. For example, the optical property of scattering causes intensity attenuation while increasing the nanosecond to subnanosecond “time of flight” of photons that are launched at the tissue surface, migrate throughout the tissues, and are detected at the tissue surface. In contrast, the optical property of absorption causes intensity attenuation, and decreases the detected photon time of flight. The extra variable of time enables differentiation of absorption from scattering properties.[31] In addition, when fluorescent contrast is added, the nanosecond lifetime provides another time-dependent contrast mechanism not available in cw measurements.[32] In fact, the fluorescent contrast measured by time-dependent methods is greater than that measured using cw techniques.[33,34]

Time-dependent methods can be categorized into time-domain and frequency-domain approaches.[35,36] As illustrated in Figs. 9(b) and 9(d), time-domain approaches consist of launching a pulse of excitation light and monitoring, as a function of time, the arrival of a broadened and attenuated emission pulse. Typically, single photon counting techniques count and time the arrival of the first arriving photon associated with a single pulse of excitation light. Hence for each photon counted, there is at least one pulse of excitation light

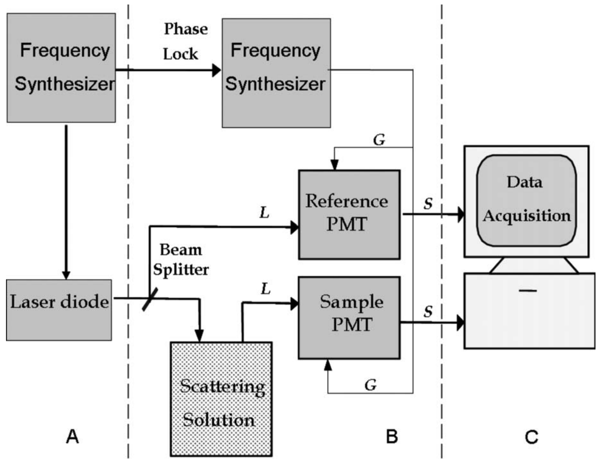

Fig. 10 Schematic of the FDPM instrumentation: (a) light source, (b) light delivery and detection, and (c) data acquisition and analysis. *L* is the detected modulated signal, *G* is the heterodyning signal with the offset frequency component, and *S* is the resulting mixed signal. Adapted from Sun et al.[71]

launched at the tissue surface, and for accurate statistics, no more than one photon can be counted for each excitation pulse launched. The time-domain measurement consists of the statistical distribution of emission photon arrival times following a pulse of excitation light. Gated integration offers a more attractive approach, in which multiple photons are counted in a small gated window of time after each consecutive excitation pulse until adequate SNR is achieved. Time-domain approaches can require significant data acquisition time, and in the authors' experience, probably are not amenable for fluorescence-enhanced optical imaging in biological tissues. In addition, the coupled integrodifferential equations that describe the distribution of fluorescent photon time of flights cannot be directly used for image recovery and must be solved in frequency space.[37] Frequency-domain approaches represent steady-state measurements conducted in frequency space and consist of 1. launching excitation light that is intensity modulated at MHz frequencies, and 2. collecting the modulated fluorescent light that is amplitude attenuated and phase shifted relative to the excitation light, as shown in Figs. 9(a) and 9(c). By scanning through the modulation frequencies, the information obtained from frequency-domain techniques can be directly related to that from time-domain techniques via Fourier transform. However, as shown next, significant information enabling tomographic reconstruction can be acquired from data taken at a single modulation frequency. In the following, we briefly describe heterodyned PMT-based measurements and homodyne measurements based on an integrating intensified CCD camera.

A schematic of a heterodyned PMT-based frequency-domain instrument is illustrated in Fig. 10. Briefly, an rf signal at modulation frequency ω is generated by a master oscillator and added to the dc current of a laser diode to produce excitation light modulated at ω. The modulated excitation light is launched into a tissue or tissue phantom at a single discrete point usually via a fiber optic or by a focused point of light. The fluorescence that results from the modulated excitation light can be collected via fiber optics located at a distant point. The fluorescent signal is also modulated and is mathematically expressed by:

$$L = L_{\mathrm{dc}} + L_{\mathrm{ac}} \cdot \cos[\omega t + \theta], \tag{1}$$

where L_{dc} is the dc component, of the fluorescent signal, L_{ac} is the ac component, and θ is the phase shift relative to the incident excitation light. It is these components that define the complex emission fluence used as input for tomographic reconstruction. Unfortunately, since L is modulated at MHz frequencies, acquisition requires mixing to reduce the high frequency to a more manageable modulation frequency for determination of L_{dc}, L_{ac}, and θ. The collected signal is either mixed at the PMT detector (as shown in Fig. 10) or at the output of an avalanche photodiode with another rf signal G that is phase locked to the master oscillator, but modulated at ω plus a kHz offset frequency of $\Delta\omega$. This signal is expressed as:

$$G = G_{\mathrm{dc}} + G_{\mathrm{ac}} \cos[(\omega + \Delta\omega)t + \theta_{\mathrm{inst}}], \tag{2}$$

where G_{dc} and G_{ac} are the dc and ac components, respectively, and θ_{instr} is an additional phase delay owing to instrumentation. The mixed signal S is simply a product of $L \times G$ and has ac components at high frequencies of ω, $2\omega + \Delta\omega$, and a low frequency component at $\Delta\omega$. On passing through a low-pass filter, the low frequency signal contains all the information describing L:

$$S = L_{\mathrm{dc}} + G_{\mathrm{dc}} + \frac{L_{\mathrm{ac}} \cdot G_{\mathrm{ac}}}{2} \cos[\Delta\omega t - \theta + \theta_{\mathrm{inst}}]. \tag{3}$$

With a matched reference detector and appropriate calibration, absolute values of L_{dc}, L_{ac}, and θ can be determined. For more detailed information on the setup in Fig. 10, see Sun et al..[38,71] Other approaches for PMT-based measurements in the frequency domain utilize a network analyzer,[39] I and Q homodyning,[40] etc., but each have employed a setup to make what we have termed "single-pixel" measurements using a single detector to collect light from a single point on the tissue phantom or surface. However, none of these approaches have been used to measure values of fluorescent L_{dc}, L_{ac}, and θ in response to excitation light illumination at a phantom or tissue surface. Unfortunately, in phantom studies using micromolar concentrations of ICG, we also found it difficult to measure L_{dc}, L_{ac}, and θ with enough SNR for tomographic reconstruction,[41] but instead found that homodyne measurements with a gain modulated CCD camera provided a method to integrate measurements for time-dependent measurements with high SNR[42] that is similar to the fluorescence lifetime imaging microscopy (FLIM) techniques devised by Lakowicz and Berndt.[43]

Figure 11(a) is a schematic of a gain-modulated CCD camera system used to acquire fluorescent, time-dependent measurements for tomographic reconstruction.[42,44–47] As in the case of heterodyned measurements, a diode light source is modulated at frequency ω. Since we are employing an area detector (i.e., a CCD camera), the modulated light from the diode can be shaped into a broad beam,[48] pattern,[49] line, or

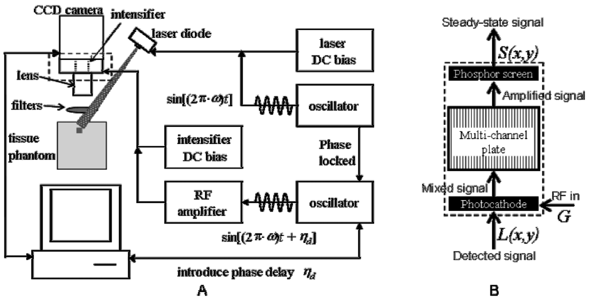

Fig. 11 (a) schematic of the homodyne intensified CCD camera system for frequency-domain measurements. The dashed box outlines the blown up region shown in (b). (b) Blow up of the intensifier, demonstrating the major regions of the intensifier and the homodyne mixing of $L(x,y)$ and G.

more conventionally, delivered to the sample via fiber optics. The fluorescence light that emanates from the x-y surface can be presented as vector $L(x,y)$:

$$L(x,y) = L_{\mathrm{dc}}(x,y) + L_{\mathrm{ac}}(x,y)\cos[(\omega t + \theta(x,y)\ ]. \tag{4}$$

The fluorescent light can be captured by an array of fiber optics or through a focusing lens for noncontact tomographic imaging using the area detector. The "master" oscillator that produces the rf signal that drives the laser diode is also phase locked by a 10-MHz signal to a "slave" oscillator, which provides another rf signal modulated at ω but phase shifted by η. This second rf signal is amplified and is used to modulate either the photocathode or MCP-in of an 18-mm-diam, NIR sensitive GEN III image intensifier. Regardless of whether it is the photocathode or MCP-in, the gain of the intensifier G is likewise given by Eq. (2) and has a dc component G_{dc}, and ac component G_{ac}, and an additional phase delay owing to instrumentation θ_{instr}.

As shown in Fig. 11(b), the incoming photons are converted to electrons at the photocathode of the intensifier, and the resulting mixed signal is amplified in the MCP prior to striking the phosphor screen to produce a pixilated signal $S(x,y)$ that is simply the product of $L(x,y)$ and G:

$$S(x,y) = L(x,y) \times G$$

$$\begin{aligned} S(x,y) = {} & L_{\mathrm{dc}}(x,y) \cdot G_{\mathrm{dc}} + L_{\mathrm{dc}}(x,y) \cdot G_{\mathrm{ac}} \cdot \cos[(\omega)t + \theta_{\mathrm{inst}} + \eta] \\ & + G_{\mathrm{dc}} \cdot L_{\mathrm{ac}}(x,y) \cdot \cos[\omega t + \theta(x,y)] \\ & + \frac{L_{\mathrm{ac}}(x,y) \cdot G_{\mathrm{ac}}}{2} \cdot \cos[-\,\theta(x,y) + \theta_{\mathrm{inst}} + \eta] \\ & + \frac{L_{\mathrm{ac}}(x,y) \cdot G_{\mathrm{ac}}}{2} \cdot \cos[(2\omega)t + \theta(x,y) + \theta_{\mathrm{inst}} + \eta]. \end{aligned} \tag{5}$$

Because the phosphor screen of the intensifier has a long time constant, it acts as a low-pass filter and a steady-state signal is ultimately registered. The signal becomes:

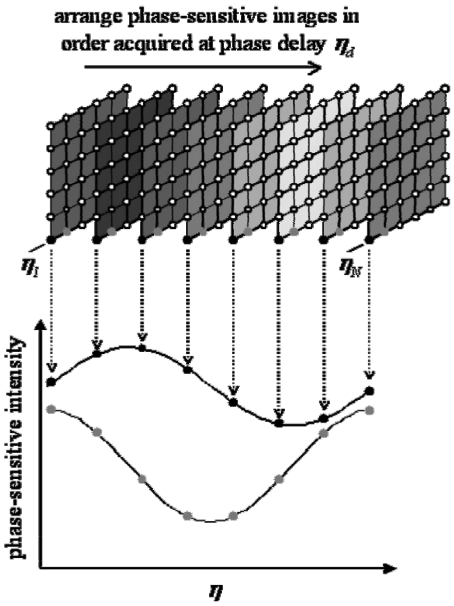

Fig. 12 Schematic illustrating homodyne data acquisition. For each phase delay introduced between $L(x,y)$ and G, an image is acquired. When plotted as a function of phase delay, the resulting intensities illustrate the modulated mixed signal $S(x,y)$, which yield amplitude and phase via Fourier transform. Reproduced from Thompson and Sevick-Muraca.[50]

$$\begin{aligned} S(x,y) = {} & L_{\mathrm{dc}}(x,y) \cdot G_{\mathrm{dc}} + \frac{L_{\mathrm{ac}}(x,y) \cdot G_{\mathrm{ac}}}{2} \cos[-\,\theta(x,y) + \theta_{\mathrm{inst}} \\ & + \eta]. \end{aligned} \tag{6}$$

The steady-state image is then collected by the CCD using lens or fiber optic coupling. The CCD integrates in time to acquire an array of measurements on a single area detector with the highest SNR. To recover $L_{\mathrm{ac}}(x,y)$ and $\theta(x,y)$, the phase lag η between the modulation of the incident laser source and the image intensifier is stepped through 360 deg. Each value of $S(x,y)$ at phase delay η defines a point on a sine wave with modulation frequency ω, as shown in Fig. 12.[50] From the Fourier transform of the zero-averaged data taken across all phase delays, the relative values of $L_{\mathrm{ac}}(x,y)$ and $\theta(x,y)$ are determined. Unfortunately, unlike the dual PMT-based system depicted in Fig. 10, there is no reference area detector. Consequently, there is no readily available referencing scheme to determine the absolute values of $L_{\mathrm{ac}}(x,y)$ and $\theta(x,y)$. Instead, values that are referenced to those at a defined position (x,y) or at the excitation wavelength are employed in an appropriately modified tomography algorithm.

The salient features that have enabled successful time-dependent measurements using the gain-modulated image intensified system are: 1. the use of camera integration at each phase delay to achieve the highest SNR; 2. the ability to collect several measurements on one area detector, that being the combination of the intensifier and CCD camera; and 3. the ability to perform noncontact illumination of excitation light using projections of patterns, lines, or points of modulated excitation light and to collect the emanating fluorescent light using lenses rather than fiber optics. It is noteworthy that the

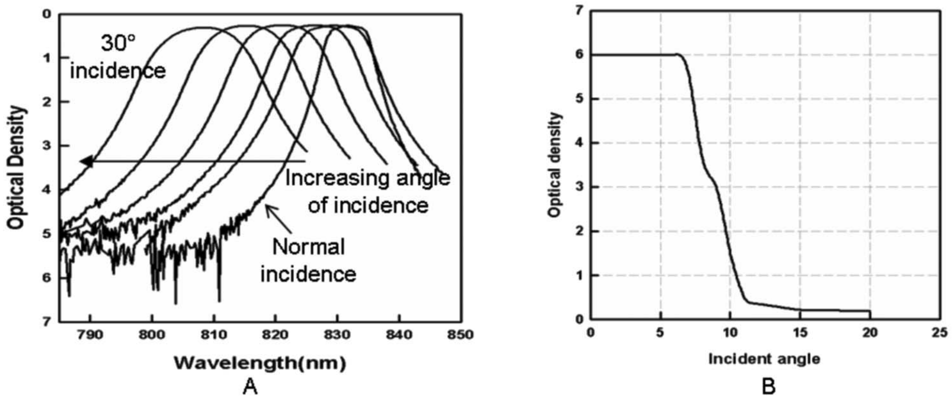

Fig. 13 (a) Optical density of 830-nm interference filter as a function of incident angle (from Andover with permission). (b) Optical density of Kaiser holographic filter as a function of incident angle (reproduced from the *Handbook of Vibrational Spectroscopy*[72] with permission).

NIR gain modulated intensified CCD camera optimized for sensitive detection of time-dependent fluorescence measurements can readily be adapted for cw imaging by simply reducing the rf power to zero. In either modality, the overall depth that can be successfully probed is dependent on the ability of photons to penetrate the tissue and the rejection of unwanted backscattered excitation photons.

Finally, a critical feature of our imaging system, whether for homodyne frequency domain or cw imaging, is the ability to enhance rejection of excitation light before reaching the photocathode of the intensifier. Early in the developmental phase, some investigators published experimental results for tomographic reconstruction of femtomolar concentrations of near-infrared dye using "leaky," low OD filters to reject excitation light in a PMT-based system (see review by Hwang et al.[17]). Unfortunately, the optimal rejection of excitation light is perhaps the greatest challenge to improving the sensitivity of fluorescence imaging systems, and requires custom holographic rejection filters designed for the laser diode source of smallest bandwidth. In addition, as seen in Fig. 13, interference filters perform poorly when light is not normally incident. Appropriate optics design to collimate incident images onto interference filters and to minimize stray light must be undertaken to achieve sensitivities necessary for molecular imaging.

Our group has defined metrics that enable comparison of the excitation light leakage between different imaging devices,[17,51] whether operated in cw or frequency-domain modes. We employ the image of the surface of an intralipid solution in the presence and absence of uniformly distributed ICG as the basis of a method to assess excitation light leakage. While we used the camera system depicted in Fig. 11 to acquire images in either cw or frequency-domain mode, the same method can be applied to any system designed to measure fluorescence emanating from biological tissue. We define excitation light leakage as the signal $S(\lambda_x)$ or average intensity values associated with the image of the scattering surface taken in the absence of ICG in the solution, while using excitation light illumination and selected optical filters to reject excitation light. The fluorescence signal $S(\lambda_m)$ is likewise averaged from the intensity values associated with the image taken in the presence of ICG in the solution. The $S(\lambda_x)$ signal represents "out of band" transmission signals, whereas the difference $S(\lambda_m)-S(\lambda_x)$ represents the "in-band" transmission signal. The transmission ratio R of the laser, filter, and lens combination is given by:

$$R(I_{\mathrm{dc}}) \text{ or } R(I_{\mathrm{ac}}) = \frac{S(\lambda_x)}{S(\lambda_m) - S(\lambda_x)}, \tag{7}$$

where $R(I_{\mathrm{dc}})$ or $R(I_{\mathrm{ac}})$ is the ratio when S is the signal measured by the average intensity I_{dc}, or the amplitude of intensity I_{ac}, respectively. A decrease in R signifies improved excitation light rejection, which leads to increased measurement sensitivity and lower noise floors. The transmission ratios of I_{dc} and I_{ac} images acquired with (solid bars) and without (nonshaded bars) collimating optics are shown in Fig. 14 as a function of distance r from the center of the 18-mm-diam photocathode. In all cases, a reduction of 51 to 75% of $R(I_{\mathrm{dc}})$ and $R(I_{\mathrm{ac}})$ occurred when collimating optics were employed. Additionally, for the uncollimated images, a departure of the incident angle from normal increases the transmission ratios $R(I_{\mathrm{dc}})$ and $R(I_{\mathrm{ac}})$ with increasing distance r from the center of the image intensifier, consistent with increasing angle of incidence on the filters. Consistent with our previous reports,[51] measurements of I_{ac} have a reduced out-of-band transmission in comparison to I_{dc}, owing to the natural frequency filtering of ambient, out-of-band light. As a matter of practice, instrument performance is quantified in our laboratories through the transmission ratio, since laser diode, filters, and misalignments can substantially impact the noise floor of fluorescence measurements. Since there is always a finite noise floor owing to excitation light leakage, the development of tomographic algorithms should account for light leakage when the fluorescent imaging agent is either not present or present in too low of a concentration to yield a signal that can overcome the noise floor.

7 Near-Infrared Tomographic Imaging in Biological Tissues

Optical tomography of biological tissues is the subject of several excellent treatises (for example, see Ref. 52) and is not reviewed in complete detail here. It is suffice to say that the

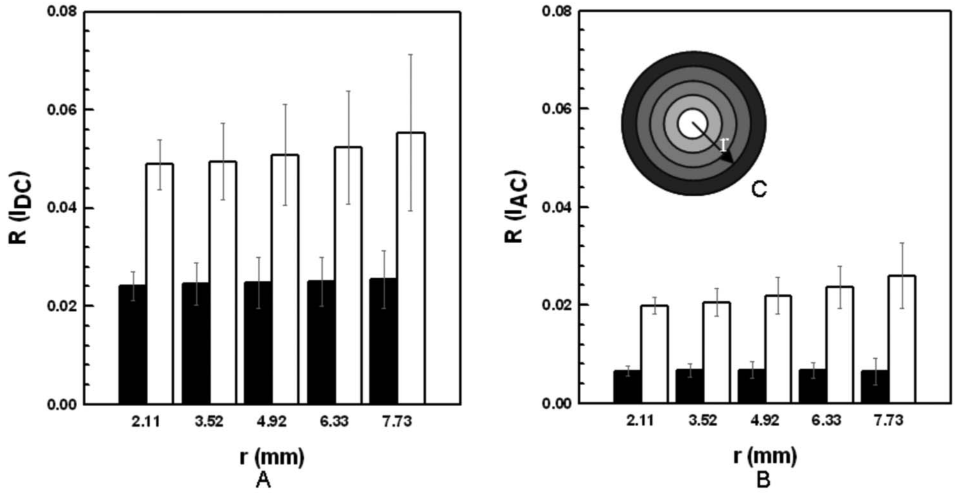

Fig. 14 Transmission ratio of (a) dc intensity $[R(I_{\mathrm{dc}})]$, and (b) ac amplitude $[R(I_{\mathrm{ac}})]$, computed from filter combination (holographic—bandpass—holographic filters) as a function of r, the distance from the center of photocathode, as shown by C. Black and white bars indicate out-of-band to in-band ratio of the imaging system with and without collimating optics, respectively. Error bars represent standard deviations of intensity with ROI. Adapted from Hwang et al.[17]

primary goal of optical tomography is to quantify agent uptake in terms of percent injection dose per gram (%ID/gm) as do SPECT and PET or in terms of relative tissue concentration. Unlike SPECT and PET, where high energy photons transit in tissues with low attenuation coefficients, optical imaging is plagued by multiple scattering, and in some cases, intense absorption, requiring the use of accurate forward models that model light propagation and generation in tissues. Given an interior optical property map, an accurate solution to the forward imaging problem must predict boundary value measurements, while the solution to the imaging (reconstruction) problem must provide an optimized interior optical property map that best matches boundary measurements. For quantitative optical tomography, an accurate forward model is required.

Most tomographic algorithm development involves the use of the diffusion approximation to the radiative equation. The limits of the diffusion approximation require that the isotropic scattering coefficient $[\mu_s' = \mu_s(1-g)]$ be much greater than the absorption coefficient, such that $\mu_s' \geqslant 10\mu_a$, and that the detector be far away from the source (>10 mean free paths). These limits generally hold true for large tissue volumes such as human breast tissue. Using the coupled diffusion equations to describe excitation light propagation and fluorescent light generation, a number of image reconstructions have been performed from experimental measurements. For example, Godavarty et al.[42] used fiber optics, as shown in Fig. 15, to deliver modulated excitation light to a clinically relevant-sized breast phantom and fiber optics to deliver the collected light to the gain-modulated image intensifier to obtain emission measurements of amplitude and phase. From these measurements, they were able to tomographically reconstruct 3-D images of fluorophore absorption cross section[42,44,46,47] as well as lifetime[45] using a Bayesian approach and an approximate extended Kalman filter algorithm.[53] Since endogenous properties do not influence measurements of phase and amplitude significantly when compared to the exogenous properties of fluorophore absorption cross section and lifetime,[53,54] anatomic heterogeneities in endogenous optical properties do not have to be determined for tomographic reconstructions. Figures 16(a) and 16(b) demonstrate recovered targets using a coarse finite element mesh (3857 unknowns) as well as a refined mesh (11,906 unknowns) from 286 measurements from three targets with TBR of 1:0. While recovery of absorption maps have been performed with less stringent TBR,[42] the results nonetheless demonstrate the importance of discretization levels on recovered image quality. Unfortunately, on increasing the number of unknowns, the accuracy in target location and resolution achieved by the inverse problem becomes more

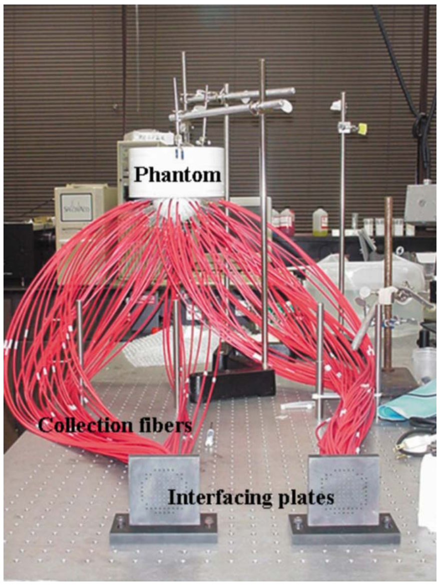

Fig. 15 Schematic of a clinically relevant breast-shaped phantom utilizing fiber optics to collect and deliver fluorescent light to the intensified CCD system. Adapted from Godavarty et al.[42]

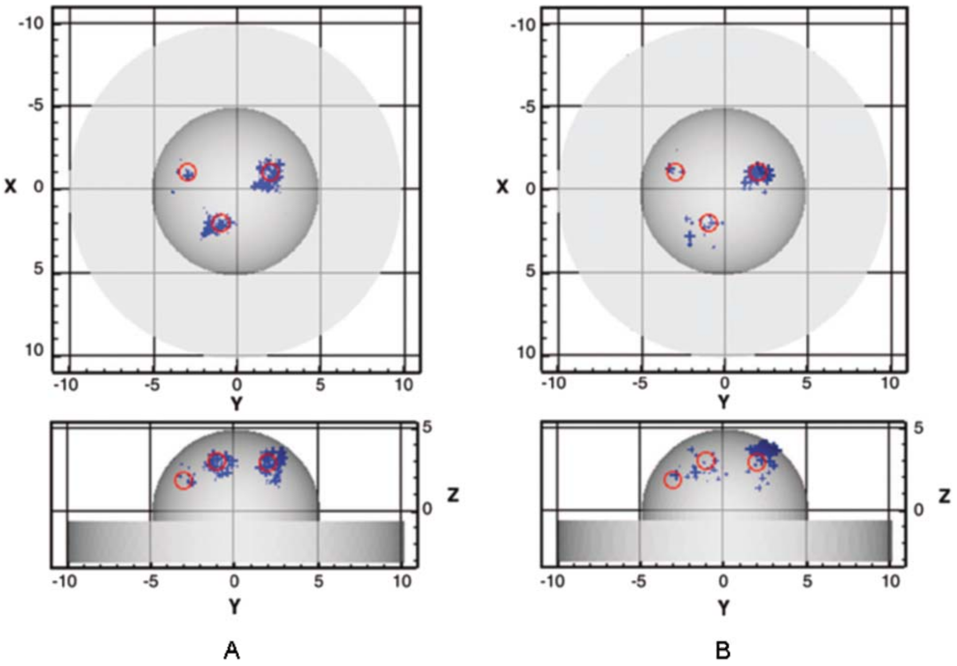

Fig. 16 Anterior (top) and lateral (bottom) views of reconstructed tissue phantoms illustrating the effect of mesh size on the accuracy of optical tomography. The actual target (0.55 cm^3 each) locations are located about 1.30 cm deep, as indicated by the solid red circles. The TBR is 1:0, and the reconstructed targets are indicated by blue points at the corresponding nodes in the finite-element mesh. The reconstruction was performed on (a) a finely discretized finite-element mesh with 11,906 unknowns, and (b) a coarse discretized finite-element mesh with 3857 unknowns. As is evident, the finer mesh produced more accurate results. Reproduced from Godavarty et al.[45] (Color online only.)

ill-posed, requiring greater computational memory and power to solve, if a solution can be achieved at all. While investigators in the areas of endogenous optical tomography use CT and MRI to segment tissue regions of unknown but uniform optical properties to reduce the number of unknowns in the inverse problem,[55,56] the anatomical features from CT and MRI cannot be expected to correspond to the presence of disease markers. While CT provides attenuation correction for PET, it is unlikely that anatomical maps will be needed for time-dependent fluorescence measurements, since anatomical heterogeneity of endogenous optical properties do not significantly impact measurements of emission phase and amplitude.[53,54] Consequently, *a priori* assignment of tissue regions representing uniform unknown fluorescent properties will not likely be appropriate for fluorescence-enhanced molecular imaging.

Another approach to reduce the unknowns in the inverse problem uses a graded, dual meshing approach in which the forward mesh is more refined near the position of incident excitation light where the steep gradient of excitation fluence is expected. The graded mesh in the forward problem insures accurate prediction, but if used for an inverse solution, would unnecessarily increase the number of unknowns. But by employing a dual meshing scheme, that is, using a refined mesh for accurate forward solutions, and a course mesh for recovery of the interior optical property map, one can mitigate computational costs without impacting forward solution accuracy. Figure 17 illustrates the conundrum between image reconstructions that employ a course grid for efficient recovery of fluorescent properties, or a refined grid that enables accurate forward solutions and parameter maps with higher resolution. Recently, using adaptive finite element strategies, Joshi et al.[57] pioneered the use of self-refining forward and inverse hexagonal meshes that automatically refine where the gradient of excitation light is steep in the forward mesh, and where the gradient of fluorescent light is steep in the inverse mesh. Lee, Jashi, and Sevick-Muraca[58] further refined adaptive finite element optical tomography by extending it to tetrahedral meshes in curvilinear geometries. Together, the adaptive meshing as well as the area detection scheme offer new opportunities for clinical imaging.

In contrast to using fiber optics to deliver emanated light to the intensified CCD camera, a lens can be employed for noncontact imaging. With the addition of time-dependent measurements, Roy and co-workers[48] have shown the ability to collect measurements from an x-y surface and reconstruct in x-y-z space. More recently, Joshi et al.[49] demonstrated that in addition to the time dependence offered by frequency-domain measurements in the x-y plane, the excitation light incident on the x-y plane can be patterned to provide spatial information to further enhance x-y-z recovery of fluorescent targets. Indeed, patterned and/or multiple sources are needed to provide unique tomographic reconstructions with accurate depth sensitivity. By coupling the adaptive finite element scheme to properly adapt the forward mesh to reflect different excitation source patterns on a 2-D surface, reconstruction of 3-D maps have been demonstrated (see Fig. 18). Future work involves accounting for and illuminating curved 2-D surfaces for accurate 3-D reconstruction.

In addition to fluorescence optical tomography in clinically relevant volumes, small animal tomography represents an

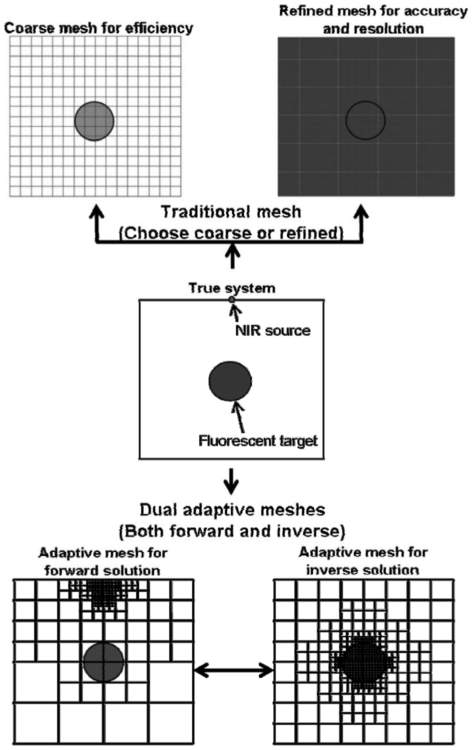

Fig. 17 Illustrates the meshing options available for tomographic reconstructions. The middle row represents the true system to be reconstructed. The top row illustrates the mesh choice, coarse or refined, that has traditionally been available. The coarse grid is more efficient to solve, but at the cost of accuracy and resolution (see Fig. 16 for a real example), while the refined mesh offers accuracy and resolution but requires significantly more computational resources, and may be unsolvable due to the increase in the ill-posed nature of the problem. The recent development of utilizing dual adaptive meshes offers the advantage of refinement in regions where it is needed without the unnecessary build-up in unknowns. In this approach, the meshes are refined between iterations when needed.

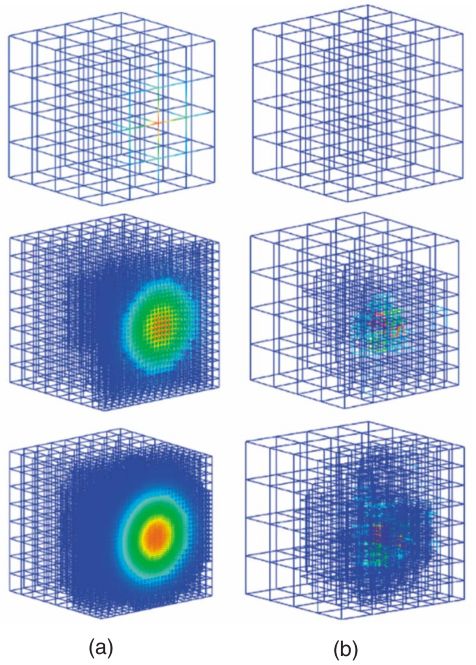

Fig. 18 Example of adaptive mesh evolution for the (a) forward and (b) inverse problems in the reconstruction of phantoms containing a single fluorescent target. Meshes are shown at the first, 11th, and 22nd Gauss-Newton iterations. The initial meshes started with 64 hexahedral elements. After five automated refinements, the final forward mesh had 116,936 elements, and the inverse mesh had 1016 elements. Reproduced from Joshi et al.[57]

important frontier for the development of therapeutic and diagnostic agents needed for personalized medicine. Tomography algorithms are currently under development for bioluminescence imaging, but are made most complicated by the facts that:1. there are no time-dependent measurements possible, and 2. endogenous optical property maps are needed to discern the difference between the low expression of a gene reporter in a tissue region of low photon attenuation and the high expression of a gene reporter in a tissue region of high photon attenuation. Tomographic algorithms associated with fluorescent gene reporters and probes that are excitable by visible wavelengths must differentiate between autofluorescence, excitation light leakage, and the signal sought for quantification. Finally, algorithms that seek to employ NIR fluorescence measurements for tomographic reconstruction have perhaps the best possible chance for validation against gold-standard nuclear imaging techniques, using dual-labeled imaging agents introduced in Sec. 5. For optical tomographic validation to succeed, an accurate forward model of light propagation and fluorescence generation is needed.

Much of the current research on optical tomography is performed on optically thick tissues where photons multiply scatter prior to detection. Small animals have a wide range of optical properties in their small volume, including diffusive regions such as the skin and highly absorptive, nondiffusive regions such as the liver. Because of the wide range of optical properties and the small volumes of interest, the diffusion approximation is not strictly valid in mice; however, several groups have successfully used the diffusion equation to reconstruct fluorophore concentration in small animals using volumetric noncontact approaches.[59–63] Further research, pioneered by Dorn,[64] and Hielscher, Alcouffe, and Barbour,[65] uses the full radiative transport equation (RTE) in optical tomography, and recently the RTE has been extended to model frequency-domain measurements in small volumes such as mice.[66,67] However, one of the remaining challenges of the RTE is the accurate prediction of the anisotropy, which describes the probability that a photon will be forward scattered. To date, the critical validation step to compare quantitative tissue concentrations of molecular species determined from small animal fluorescence tomography (diffusion or RTE based) and gold-standard nuclear techniques remain to be completed.

8 Clinical Translation of Near-Infrared Imaging: Prospects

In the earlier sections, we tried to provide a bird's eye view of the development of molecularly targeting agents, imaging devices, and tomographic reconstruction algorithms that make possible a role for molecular optical imaging in personalized medicine. However, translation of optical molecular imaging may be especially daunting, given that there are no approved imaging devices or agents currently available commercially. As such, before a "first-in-humans" molecular optical imaging agent is introduced in an investigational study and the unknown "risk" of human administration is accepted, the potential benefit of actually being able to measure fluorescent signals emanating from human tissues needs to be demonstrated. If an imaging device can be demonstrated to provide a clinically meaningful signal under microdosing conditions, then the chance for an adverse event associated with the investigational imaging agent is mitigated. The United States Food and Drug Administration (FDA) defines microdose administration as less than 100 μg of a nonbiological material, $\leqslant$30 nmoles of a protein-based agent, or if using a labeled therapeutic, $1/100$ of the pharmacological dose.[68]

In our work, we have capitalized on the safety record of ICG, which is approved for intravenous administration for assessing hepatic function and retinopathy, but not for the indication of fluorescence imaging. Nonetheless, ICG is an NIR fluorophore that can be used to test the sensitivity of the gain-modulated image intensified CCD system depicted in Fig. 11, in an off-label use approved by the FDA. In our ongoing program to develop dual-labeled imaging agents for nodal staging of cancer, we used IC-green in a dose escalating fashion to image the lymphatics via subcutaneous or intradermal injections in breast cancer patients undergoing standard-of-care sentinel lymph node mapping. These patients were also injected with 99m-Technetium sulfur colloid for gamma scintigraphy to locate sentinel nodes for surgical resection and biopsy to confirm absense or presence of cancer. Our ultimate goal is to use NIR optical molecular imaging agents to detect cancer positive lymph nodes noninvasively to alleviate the need for surgical resection to provide prognostic indicators. To date, we have found that when ICG doses are greater than 10 μg, we can image propulsive lymph trafficking from the site of injection to the sentinel and axillary lymph nodes[69] with frame rates of 100 to 800 msec. Furthermore, we confirm ICG lymph trafficking from the ICG fluorescence detected in resected lymph nodes. Spurred by our results, we have recently begin using nonspecific ICG and our device to image lymph flow in normal subjects and in breast cancer survivors who suffer from arm lymphedema.[70] With as little as 100 μg of ICG, we are able for the first time to quantitatively image lymph velocity in major lymph bundles and deep lymph vessels that drain into lymph node basins (for example, see Fig. 19). The dynamic imaging of lymph flow results from the high photon count rate, coupled with the low noise floors associated with NIR excitation and with proper design, allowing for integration and efficient excitation light rejection.

While ICG will not enable the molecular imaging of cancer-positive lymph nodes, as perhaps the trastuzumab-based imaging agent described in this series and by Sampath et al.,[25] the study nonetheless allows us to determine that microdosing of NIR molecular targeting agents will provide a signal that can be captured by an NIR sensitive imaging device. With the validation of potential benefit of our imaging device, our next steps will be to validate a "first-in-humans" imaging agent using the dual-labeled approach, allowing direct comparison between NIR and the gold standard of nuclear imaging.

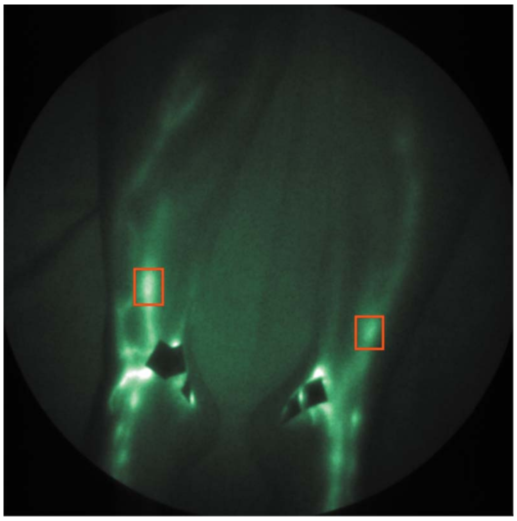

Fig. 19 Image acquired of real-time lymph transport in the legs. The black marks are small pieces of plastic used to cover the injection sights. The green streaks are lymphatic vessels, and the bright spots in the red squares are packets of lymph that are transiting from the ankles to the inguinal nodes. (Color online only.)

Acknowledgments

We acknowledge the contributions from all past members of the Photon Migration Laboratory from Vanderbilt University, Purdue University, Texas A and M University, and Baylor College of Medicine beginning in 1991: Christina L. (Burch) Hutchinson, Tamara L. Troy, Steven Richter, Daniel Hawrysz, Jangwoen Lee, Zhigang Sun, Alan Thompson, Anuradha Godavarty, Yingqing Huang, Michael Gurfinkel, Eddy Kuwana, Tianshu Pan, Amit Joshi, Jessica Houston, Sarabjyot Singh Dali, John C. Rasmussen, Feng Liang, Kildong Hwang, Amit Sahu, Sunkuk Kwon, Ruchi Sharma, Lakshmi Sampath, Lee Suddeath, Kavi Sharma, Lena L. Nelson-Larry, Jeffrey Kao, Joseph Pierce, Guadiana Lopez, Alvin Chen, Sharnay Torrance, Dilip Y. Paithankar, Jeffery Reynolds, Huabei Jiang, Rajesh Shinde, Ganesh Balgi, Ralph Mayer, Sukanta Banerjee, Ranadhir Roy, Kristen Adams, Jae Hoon Lee, Pier-Anne LaChance, Ranjani Ranganathan, Cynthia Davies-Venn, and Sergy Lemeshko. We acknowledge the assistance of Jessica Nollkamper and the support of R01 CA112679.

References

1. R. Weissleder, "Molecular imaging in cancer," *Science* **312**(5777), 1168–1171 (2006).
2. H. R. Herschman, "Molecular imaging: looking at problems, seeing solutions," *Science* **302**(5645), 605–608 (2003).
3. M. Rudin and R. Weissleder, "Molecular imaging in drug discovery and development," *Nat. Rev. Drug Discovery* **2**(2), 123–131 (2003).
4. R. G. Blasberg and J. G. Tjuvajev, "Molecular-genetic imaging: current and future perspectives," *J. Clin. Invest.* **111**(11), 1620–1629 (2003).
5. T. F. Massoud and S. S. Gambhir, "Molecular imaging in living subjects: seeing fundamental biological processes in a new light," *Genes Dev.* **17**(5), 545–580 (2003).
6. M. E. Phelps, "PET: molecular imaging and its biological applications," in *Primer of Diagnotics Imaging*, R. Weissleder, J. M. Wittenberg, and M. G. Harisinghani, Eds., Springer, New York (2003).
7. R. Weissleder, J. M. Wittenberg, and M. G. Harisinghani, *Primer of Diagnostic Imaging*, 3rd ed., Mosby, Philadelphia (2003).
8. S. S. Gambhir, J. R. Barrio, L. Wu, M. Iyer, M. Namavari, N. Satya-

murthy, E. Bauer, C. Parrish, D. C. MacLaren, A. R. Borghei, L. A. Green, S. Sharfstein, A. J. Berk, S. R. Cherry, M. E. Phelps, and H. R. Herschman, "Imaging of adenoviral-directed herpes simplex virus type 1 thymidine kinase reporter gene expression in mice with radiolabeled ganciclovir," *J. Nucl. Med.* **39**(11), 2003–2011 (1998).

9. J. G. Tjuvajev, M. Doubrovin, T. Akhurst, S. D. Cai, J. Balatoni, M. M. Alauddin, R. Finn, W. Bornmann, H. Thaler, P. S. Conti, and R. G. Blasberg, "Comparison of radiolabeled nucleoside probes (FIAU, FHBG, and FHPG) for PET imaging of HSV1-tk gene expression," *J. Nucl. Med.* **43**(8), 1072–1083 (2002).
10. M. Iyer, J. R. Barrio, M. Namavari, E. Bauer, N. Satyamurthy, K. Nguyen, T. Toyokuni, M. E. Phelps, H. R. Herschman, and S. S. Gambhir, "8-[F-18]fluoropenciclovir: an improved reporter probe for imaging HSV1-tk reporter gene expression in vivo using PET," *J. Nucl. Med.* **42**(1), 96–105 (2001).
11. T. Groot-Wassink, E. O. Aboagye, M. Glaser, N. R. Lemoine, and G. Vassaux, "Adenovirus biodistribution and noninvasive imaging of gene expression in vivo by positron emission tomography using human sodium/iodide symporter as reporter gene," *Hum. Gene Ther.* **13**(14), 1723–1735 (2002).
12. T. Petrich, H. J. Helmeke, G. J. Meyer, W. H. Knapp, and E. Potter, "Establishment of radioactive astatine and iodine uptake in cancer cell lines expressing the human sodium/iodide symporter," *Eur. J. Nucl. Med. Mol. Imaging* **29**(7), 842–854 (2002).
13. J. H. Shin, J. K. Chung, J. H. Kang, Y. J. Lee, K. I. Kim, Y. So, J. M. Jeong, D. S. Lee, and M. C. Lee, "Noninvasive imaging for monitoring of viable cancer cells using a dual-imaging reporter gene," *J. Nucl. Med.* **45**(12), 2109–2115 (2004).
14. T. Groot-Wassink, E. O. Aboagye, Y. Wang, N. R. Lemoine, A. J. Reader, and G. Vassaux, "Quantitative imaging of Na/I symporter transgene expression using positron emission tomography in the living animal," *Mol. Ther.* **9**(3), 436–442 (2004).
15. C. H. Contag, S. D. Spilman, P. R. Contag, M. Oshiro, B. Eames, P. Dennery, D. K. Stevenson, and D. A. Benaron, "Visualizing gene expression in living mammals using a bioluminescent reporter," *Photochem. Photobiol.* **66**(4), 523–531 (1997).
16. K. E. Adams, S. Ke, S. Kwon, F. Liang, Z. Fan, Y. Lu, K. Hirschi, M. E. Mawad, M. A. Barry, and E. M. Sevick-Muraca, "Comparison of visible and near-infrared wavelength-excitable fluorescent dyes for molecular imaging of cancer," *J. Biomed. Opt.* **12**(2), 020417-1–024017-9 (2007).
17. K. Hwang, J. P. Houston, J. C. Rasmussen, A. Joshi, S. Ke, C. Li, and E. M. Sevick-Muraca, "Improved excitation light rejection enhances small-animal fluorescent optical imaging," *Mol. Imaging* **4**(3), 194–204 (2005).
18. W. Wang, S. Ke, S. Kwon, S. Yallampalli, A. G. Cameron, K. E. Adams, M. E. Mawad, and E. M. Sevick-Muraca, "A new optical and nuclear dual-labeled imaging agent targeting interleukin 11 receptor alpha-chain," *Bioconjugate Chem.* **18**(2), 397–402 (2007).
19. W. Wang, J. S. McMurray, Q. Wu, M. L. Campbell, and C. Li, "Convenient solid-phase synthesis of diethylenetriaminepenta-acetic acid (DTPA)-conjugated cyclic RGD peptide analogues," *Cancer Biother. Radiopharm.* **20**(5), 547–556 (2005).
20. J. P. Houston, S. Ke, W. Wang, C. Li, and E. M. Sevick-Muraca, "Quality analysis of in vivo near-infrared fluorescence and conventional gamma images acquired using a dual-labeled tumor-targeting probe," *J. Biomed. Opt.* **10**(5), 054010 (2005).
21. C. Li, W. Wang, Q. P. Wu, K. Shi, J. P. Houston, E. M. Sevick-Muraca, L. Dong, D. Chow, C. Charnsangavej, and J. G. Gelovani, "Dual optical and nuclear imaging in human melanoma xenografts using a single targeted imaging probe," *Nucl. Med. Biol.* **33**(3), 349–358 (2006).
22. S. Kwon, S. Ke, J. P. Houston, W. Wang, Q. Wu, C. Li, and E. M. Sevick-Muraca, "Imaging dose-dependent pharmacokinetics of an RGD-fluorescent dye conjugate targeted to alpha v beta 3 receptor expressed in Kaposi's sarcoma," *Mol. Imaging* **4**(2), 75–87 (2005).
23. M. Gurfinkel, S. Ke, W. Wang, C. Li, and E. M. Sevick-Muraca, "Quantifying molecular specificity of alphavbeta3 integrin-targeted optical contrast agents with dynamic optical imaging," *J. Biomed. Opt.* **10**(3), 034019 (2005).
24. S. Ke, X. Wen, M. Gurfinkel, C. Charnsangavej, S. Wallace, E. M. Sevick-Muraca, and C. Li, "Near-infrared optical imaging of epidermal growth factor receptor in breast cancer xenografts," *Cancer Res.* **63**(22), 7870–7875 (2003).
25. L. Sampath, S. Kwon, S. Ke, W. Wang, R. Schiff, M. E. Mawad, and E. M. Sevick-Muraca, "Dual-labeled transtuzumab-based imaging agent for the detection of Human Epidermal Growth Factor Receptor-2 (HER2) overexpression in breast cancer," *J. Nucl. Med.* (cover illustration), **48**, 1501–1510 (2007).
26. Z. Zhang and S. Achilefu, "Spectral properties of pro-multimodal imaging agents derived from a NIR dye and a metal chelator," *Photochem. Photobiol.* **81**(6), 1499–1504 (2005).
27. H. Xu, K. Baidoo, A. J. Gunn, C. A. Boswell, D. E. Milenic, P. L. Choyke, and M. W. Brechbiel, "Design, synthesis, and characterization of a dual modality positron emission tomography and fluorescence imaging agent for monoclonal antibody tumor-targeted imaging," *J. Med. Chem.* **50**(19), 4759–4765 (2007).
28. R. H. Adams, K. E. Adams, S. . Ke, S. . Kwon, F. . Liang, Z. . Fan, Y. . Lu, K. . Hirschi, M. E. Mawad, M. E. Barry, and E. M. Sevick-Muraca, "Comparison of visible and near-infrared wavelength excitable fluorescent dyes for molecular imaging of cancer," *J. Biomed. Opt.* **12**, 024017 (2007).
29. Z. Medarova, W. Pham, Y. Kim, G. Dai, and A. Moore, "In vivo imaging of tumor response to therapy using a dual-modality imaging strategy," *Int. J. Cancer* **118**(11), 2796–2802 (2006).
30. E. M. C. Hillman and A. Moore, "All-optical anatomical co-registration for molecular imaging of small animals using dynamic contrast," *Nat. Photonics* **1**(9), 526–530 (2007).
31. E. M. Sevick, B. Chance, J. Leigh, S. Nioka, and M. Maris, "Quantitation of time- and frequency-resolved optical spectra for the determination of tissue oxygenation," *Anal. Biochem.* **195**(2), 330–351 (1991).
32. D. Y. Paithankar, A. U. Chen, B. W. Pogue, M. S. Patterson, and E. M. Sevick-Muraca, "Imaging of fluorescent yield and lifetime from multiply scattered light re-emitted from tissues and other random media," *Appl. Opt.* **36**, 2260–2272 (1997).
33. E. M. Sevick-Muraca, G. Lopez, T. L. Troy, J. S. Reynolds, and C. L. Hutchinson, "Fluorescence and absorption contrast mechanisms for biomedical optical imaging using frequency-domain techniques," *Photochem. Photobiol.* **66**, 55–64 (1997).
34. X. Li, B. Chance, and A. G. Yodh, "Fluorescent heterogeneities in turbid media: limits for detection, characterization, and comparison with absorption," *Appl. Opt.* **37**(28), 6833–6844 (1998).
35. D. J. Hawrysz and E. M. Sevick-Muraca, "Developments toward diagnostic breast cancer imaging using near-infrared optical measurements and fluorescent contrast agents," *Neoplasia* **2**(5), 388–417 (2000).
36. E. M. Sevick-Muraca, J. P. Houston, and M. Gurfinkel, "Fluorescence-enhanced, near infrared diagnostic imaging with contrast agents," *Curr. Opin. Chem. Biol.* **6**(5), 642–650 (2002).
37. R. Richards-Kortum and E. Sevick-Muraca, "Quantitative optical spectroscopy for tissue diagnosis," *Annu. Rev. Phys. Chem.* **47**, 555–606 (1996).
38. Z. G. Sun, Y. Q. Huang, and E. M. Sevick-Muraca, "Precise analysis of frequency domain photon migration measurement for characterization of concentrated colloidal suspensions," *Rev. Sci. Instrum.* **73**(2), 383–393 (2002).
39. N. Shah, A. Cerussi, C. Eker, J. Espinoza, J. Butler, J. Fishkin, R. Hornung, and B. Tromberg, "Noninvasive functional optical spectroscopy of human breast tissue," *Proc. Natl. Acad. Sci. U.S.A.* **98**(8), 4420–4425 (2001).
40. B. Chance, M. Cope, E. Gratton, N. Ramanujam, and B. Tromberg, "Phase measurement of light absorption and scatter in human tissue," *Rev. Sci. Instrum.* **69**(10), 3457–3481 (1998).
41. J. Lee and E. M. Sevick-Muraca, "Three-dimensional fluorescence enhanced optical tomography using referenced frequency-domain photon migration measurements at emission and excitation wavelengths," *J. Opt. Soc. Am. A Opt. Image Sci. Vis* **19**(4), 759–771 (2002).
42. A. Godavarty, M. J. Eppstein, C. Zhang, S. Theru, A. B. Thompson, M. Gurfinkel, and E. M. Sevick-Muraca, "Fluorescence-enhanced optical imaging in large tissue volumes using a gain-modulated ICCD camera," *Phys. Med. Biol.* **48**(12), 1701–1720 (2003).
43. J. R. Lakowicz and K. W. Berndt, "Lifetime-selective fluorescence imaging using an Rf phase-sensitive camera," *Rev. Sci. Instrum.* **62**(7), 1727–1734 (1991).
44. A. Godavarty, M. J. Eppstein, C. Zhang, and E. M. Sevick-Muraca, "Detection of single and multiple targets in tissue phantoms with fluorescence-enhanced optical imaging: feasibility study," *Radiology* **235**(1), 148–154 (2005).

45. A. Godavarty, E. M. Sevick-Muraca, and M. J. Eppstein, "Three-dimensional fluorescence lifetime tomography," *Med. Phys.* **32**(4), 992–1000 (2005).
46. A. Godavarty, A. B. Thompson, R. Roy, M. Gurfinkel, M. J. Eppstein, C. Zhang, and E. M. Sevick-Muraca, "Diagnostic imaging of breast cancer using fluorescence-enhanced optical tomography: phantom studies," *J. Biomed. Opt.* **9**(3), 488–496 (2004).
47. A. Godavarty, C. Zhang, M. J. Eppstein, and E. M. Sevick-Muraca, "Fluorescence-enhanced optical imaging of large phantoms using single and simultaneous dual point illumination geometries," *Med. Phys.* **31**(2), 183–190 (2004).
48. R. Roy, A. B. Thompson, A. Godavarty, and E. M. Sevick-Muraca, "Tomographic fluorescence imaging in tissue phantoms: a novel reconstruction algorithm and imaging geometry," *IEEE Trans. Med. Imaging* **24**(2), 137–154 (2005).
49. A. Joshi, W. Bangerth, K. Hwang, J. Rasmussen, and E. M. Sevick-Muraca, "Plane-wave fluorescence tomography with adaptive finite elements," *Opt. Lett.* **31**(2), 193–195 (2006).
50. A. B. Thompson and E. M. Sevick-Muraca, "Near-infrared fluorescence contrast-enhanced imaging with intensified charge-coupled device homodyne detection: measurement precision and accuracy," *J. Biomed. Opt.* **8**(1), 111–120 (2003).
51. J. P. Houston, A. B. Thompson, M. Gurfinkel, and E. M. Sevick-Muraca, "Sensitivity and depth penetration of continuous wave versus frequency-domain photon migration near-infrared fluorescence contrast-enhanced imaging," *Photochem. Photobiol.* **77**(4), 420–430 (2003).
52. S. R. Arridge, "Optical tomography in medical imaging," *Inverse Probl.* **15**(2), R41–R93 (1999).
53. M. J. Eppstein, D. J. Hawrysz, A. Godavarty, and E. M. Sevick-Muraca, "Three-dimensional, Bayesian image reconstruction from sparse and noisy data sets: near-infrared fluorescence tomography," *Proc. Natl. Acad. Sci. U.S.A.* **99**(15), 9619–9624 (2002).
54. A. K. Sahu, A. Joshi, R. Roy, and E. M. Sevick-Muraca, "Evaluation of anatomical structure and nonuniform distribution of imaging agent in near-infrared fluorescence-enhanced optical tomography," *Opt. Express* **13**(25), 10182–10199 (2005).
55. J. Chang, H. L. Graber, P. C. Koo, R. Aronson, S. L. Barbour, and R. L. Barbour, "Optical imaging of anatomical maps derived from magnetic resonance images using time-independent optical sources," *IEEE Trans. Med. Imaging* **16**(1), 68–77 (1997).
56. B. Brooksby, B. W. Pogue, S. Jiang, H. Dehghani, S. Srinivasan, C. Kogel, T. D. Tosteson, J. Weaver, S. P. Poplack, and K. D. Paulsen, "Imaging breast adipose and fibroglandular tissue molecular signatures by using hybrid MRI-guided near-infrared spectral tomography," *Proc. Natl. Acad. Sci. U.S.A.* **103**(23), 8828–8833 (2006).
57. A. Joshi, W. Bangerth, and E. M. Sevick-Muraca, "Adaptive finite element based tomography for fluorescence optical imaging in tissue," *Opt. Express* **12**(22), 5402–5417 (2004).
58. J. H. Lee, A. Joshi, and E. M. Sevick-Muraca, "Fully adaptive finite element based tomography using tetrahedral dual meshing for fluorescence enhanced optical imaging in tissue," *Opt. Express* **15**(11), 6954–6974 (2007).
59. J. Q. Chen, C. H. Tung, U. Mahmood, V. Ntziachristos, R. Gyurko, M. C. Fishman, P. L. Huang, and R. Weissleder, "In vivo imaging of proteolytic activity in atherosclerosis," *Circulation* **105**(23), 2766–2771 (2002).
60. E. E. Graves, R. Weissleder, and V. Ntziachristos, "Fluorescence molecular imaging of small animal tumor models," *Curr. Mol. Med.* **4**(4), 419–430 (2004).
61. V. Ntziachristos, C. H. Tung, C. Bremer, and R. Weissleder, "Fluorescence molecular tomography resolves protease activity in vivo," *Nat. Med.* **8**(7), 757–760 (2002).
62. E. A. Schellenberger, A. Bogdanov, A. Petrovsky, V. Ntziachristos, R. Weissleder, and L. Josephson, "Optical imaging of apoptosis as a biomarker of tumor response to chemotherapy," *Neoplasia* **5**(3), 187–192 (2003).
63. G. Zacharakis, H. Kambara, H. Shih, J. Ripoll, J. Grimm, Y. Saeki, R. Weissleder, and V. Ntziachristos, "Volumetric tomography of fluorescent proteins through small animals in vivo," *Proc. Natl. Acad. Sci. U.S.A.* **102**(51), 18252–18257 (2005).
64. O. Dorn, "A transport-backtransport method for optical tomography," *Inverse Probl.* **14**(5), 1107–1130 (1998).
65. A. H. Hielscher, R. E. Alcouffe, and R. L. Barbour, "Comparison of finite-difference transport and diffusion calculations for photon migration in homogeneous and heterogeneous tissues," *Phys. Med. Biol.* **43**(5), 1285–1302 (1998).
66. A. Joshi, J. C. Rasmussen, E. M. Sevick-Muraca, T. A. Wareing, and J. . McGhee, "Radiative transport based frequency domain fluorescence tomography," *Phys. Med. Biol.* **53**(8), 2069–2088 (2008).
67. K. Ren, G. S. Abdoulaev, G. Bal, and A. H. Hielscher, "Algorithm for solving the equation of radiative transfer in the frequency domain," *Opt. Lett.* **29**(6), 578–580 (2004).
68. "Guidance for industry, investigators, and reviewers: exploratory IND Studies," in *CDER* (Center for Drug Evaluation and Research), Food and Drug Administration (Jan. 2006).
69. E. M. Sevick-Muraca, R. Sharma, J. C. Rasmussen, M. V. Marshall, J. A. Wendt, H. Q. Pham, E. Bonefas, J. P. Houston, L. Sampath, K. E. Adams, D. K. Blanchard, R. E. Fisher, S. Chiang, R. Elledge, and M. E. Mawad, "Imaging of lymph flow in breast cancer patients after microdose administration of a near-infrared fluorophore," *Radiology* **246**(3), 734–741 ().
70. R. Sharma, J. C. Rasmussen, M. V. Marshall, J. A. Wendt, C. E. Fife, L. Smith, E. Maus, and E. M. Sevick-Muraca, "Imaging lymph flow in humans" (unpublished).
71. X. Sun, A. J. Annala, S. S. Yaghoubi, J. R. Barrio, K. N. Nguyen, T. Toyokuni, N. Satyamurthy, M. Namavari, M. E. Phelps, H. R. Herschman, and S. S. Gambhir, "Quantitative imaging of gene induction in living animals," *Gene Ther.* **8**(20), 1572–1579 (2001).
72. H. Owen, "Volume phase holographic optical elements," *Handbook of Vibrational Spectroscopy*, pp. 482–489, Wiley, New York (2002).